

Manipulating multiple optical parametric processes in photonic topological insulatorsZhen Jiang,^{1,2,*} Bo Ji,^{1,2,*} Yanghe Chen,^{1,2} Chun Jiang,^{1,†} and Guangqiang He^{1,2,‡}¹State Key Laboratory of Advanced Optical Communication Systems and Networks, Department of Electronic Engineering, Shanghai Jiao Tong University, Shanghai 200240, China²SJTU Pinghu Institute of Intelligent Optoelectronics, Department of Electronic Engineering, Shanghai Jiao Tong University, Shanghai 200240, China (Received 21 February 2024; revised 12 April 2024; accepted 26 April 2024; published 13 May 2024)

Topological quantum optics has endowed integrated quantum devices with novel functionalities, including unidirectional transport and immunity to structural defects. Here we propose topological interfaces that support two distinct edge modes with different frequency ranges. The nonlinear four-wave mixing processes in the topological interfaces lead to the generation of signal and idler photons, each corresponding to distinct edge modes. By designing a diamondlike topological structure, we can couple the signal and idler photons into opposite branches, leading to spatial separation of the photon pairs. This behavior enables on-chip generation and flexible control of the topological biphoton states. More importantly, the biphoton states are inborn topologically protected, showing robustness against sharp bends and disorders. Our proposal offers the possibility of robust, multifunctional topological quantum devices, which may find applications in quantum information processing.

DOI: [10.1103/PhysRevB.109.174110](https://doi.org/10.1103/PhysRevB.109.174110)**I. INTRODUCTION**

The burgeoning field of on-chip quantum light sources has been undergoing revolutionized development thanks to the advancements in nanofabrication technologies. Significant advances in reducing the size and improving the stability through photonic integrated circuits have played a pivotal role in enabling on-chip generation and control of quantum light sources [1]. These improvements have supported more complex and expanding quantum operations, which are crucial for the progress in quantum computing [2,3], quantum communication [4–6], and quantum sensing [7,8]. Two key aspects of on-chip quantum light sources are the amplification of light signals and the generation of entangled photon pairs. Implementing on-chip multifunctional quantum capabilities simultaneously requires precise dispersion engineering and specific materials and is still challenging from a certain perspective.

In parallel, the integration of topological phases into quantum systems is enhanced by the robust guidance and manipulation of light and holds great potential as a cutting-edge and promising area of research [9–11]. This approach is key to the stable generation and transport of quantum states. Topological phases possess a topological nature that provides quantum states with robustness against structural imperfections and disorders. In particular, there have been significant advancements in this field, such as the emergence of topological quantum emitters [12,13], topological quantum interference [14,15], topological biphoton states [16–18], and even topological quantum frequency combs [19,20]. At the

same time, emerging advances in topological nonlinear optics also promise topological protection of complex nonlinear processes [21–26]. A significant amount of research has focused on the development of quantum light sources in topological optical systems. However, the study of multifunctional quantum devices in topological photonic systems remains unexplored.

Here we propose integrated topological quantum devices that perform two functions, including optical parametric amplification (OPA) and the entangled biphoton state generation. We demonstrate that a sandwich topological interface emulating the quantum valley Hall (QVH) effect can support two distinct edge modes with different frequency ranges. Using a diamondlike topological structure, we can couple these two edge modes to opposite branches. This allows the spatial separation of signal and idler photons generated from four-wave mixing (FWM) processes. We show that this topological device supports multiple optical parametric processes (OPPs) and can perform two functions: OPA and the generation of continuous frequency entangled biphoton states. Moreover, these biphoton states are robust against defects and sharp bends due to the topological protection of the QVH effect. Our approach expands the potential for on-chip, robust, and multifunctional topological quantum devices and paves the way for new research paths in quantum optics.

II. RESULTS**A. Topological edge modes in kagome lattice**

The discovery of the photonic kagome lattice provides a feasible framework for the controllable design of higher-order valley-Hall edge modes [27,28]. Here we explore a two-dimensional topological kagome lattice that supports the generation and flexible control of photonic topological

*These authors contributed equally to this work.

†cjiang@sjtu.edu.cn

‡gqhe@sjtu.edu.cn

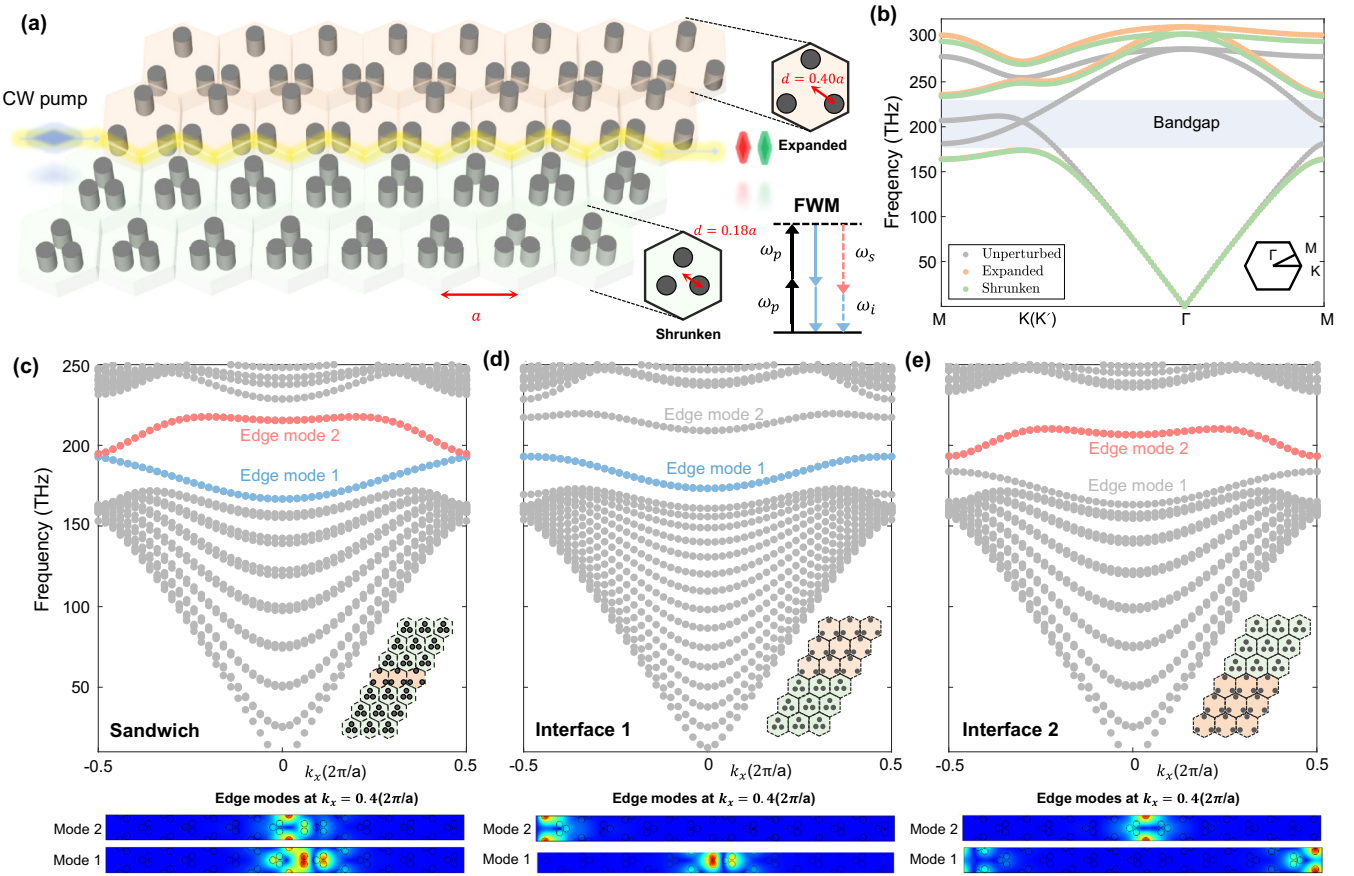


FIG. 1. (a) Scheme of topological design supporting the generation of FWM processes is composed of shrunken ($d = 0.18a$) and expanded ($d = 0.40a$) kagome lattices with C_3 symmetry. (b) Band diagrams of unperturbed (gray dots), shrunken (green dots), and expanded (orange dots) kagome lattices, respectively. Calculated dispersion curves for the (c) sandwich topological interface, (d) topological interface 1, and (e) topological interface 2, respectively. The insets in the lower right corner show schematics of three interfaces composed of shrunken (green region) and expanded (orange region) kagome lattices. The lower insets show the electric field distributions for two edge modes.

quantum states. As depicted in Fig. 1(a), a topological design supporting FWM processes is composed of two kagome lattices (with a lattice constant of $a = 480$ nm) formed by the silicon cylinders ($\epsilon = 12$) in the air background ($\epsilon_0 = 1$). The silicon cylinder has a radius of $0.13a$ and an infinite thickness. The effective topological transition is performed by expanding or shrinking an unperturbed kagome lattice. Figure 1(b) shows the band structures of unperturbed (gray dots), shrunken (green dots), and expanded ($d = 0.40a$) kagome lattices, respectively. Due to the high symmetry of unperturbed kagome lattices, a Dirac-like degeneracy appears at the two high symmetry points (K and K' valleys) of the Brillouin zone [28]. The deformation of the unperturbed kagome lattice leads to a complete photonic band gap and band inversion mechanism. Note that the band structures of shrunken ($d = 0.18a$) and expanded ($d = 0.40a$) kagome lattices do not overlap perfectly; this is because of the shifts of the dielectric cylinders are not identical.

The kagome lattice exhibits three mirror symmetries: M_x for the x axis and M_{\pm} for the two lines obtained by rotating the x axis by $\pm 2\pi/3$ [29]. The polarization along the x_i axis represents the expectation value of the position with $p_i = \frac{1}{S} \int_{\text{BZ}} A_i d^2\mathbf{k}$, where $A_i = -i\langle \psi | \partial_{k_i} | \psi \rangle$ denotes the Berry connection with $x_i = x, y$ [29]. The topological bulk

polarization describes the shift of the average position of the Wannier center from the center of the unit cell. It is noted that the topological bulk difference of shrunken and expanded kagome lattices corresponds to $P = (0, 0)$ and $P = (1/3, 1/3)$, respectively, which denotes a trivial and nontrivial case, respectively [30].

Due to the bulk-boundary correspondence, the nontrivial polarization difference leads to topological edge states localized at boundaries between the shrunken and expanded kagome lattices. Furthermore, for a finite structure, the deformed kagome lattice is expected to exhibit higher-order topological states such as zero-dimensional corner states [28]. Here we consider a sandwichlike topological interface consisting of a domain of expanded kagome lattices sandwiched between two domains of shrunken kagome lattices. The calculated band structure for this sandwich topological interface is shown in Fig. 1(c). The dispersion curve reveals the presence of two edge modes localized in the topological band gap. Furthermore, it leads to an extensive bandwidth exceeding 40 THz. The lower inset illustrates that these two modes are exclusively confined to the distinct inner boundaries between two types of kagome lattices. This behavior arises from the presence of two boundaries in the sandwich topological interface, which correspond to two topological transitions in the

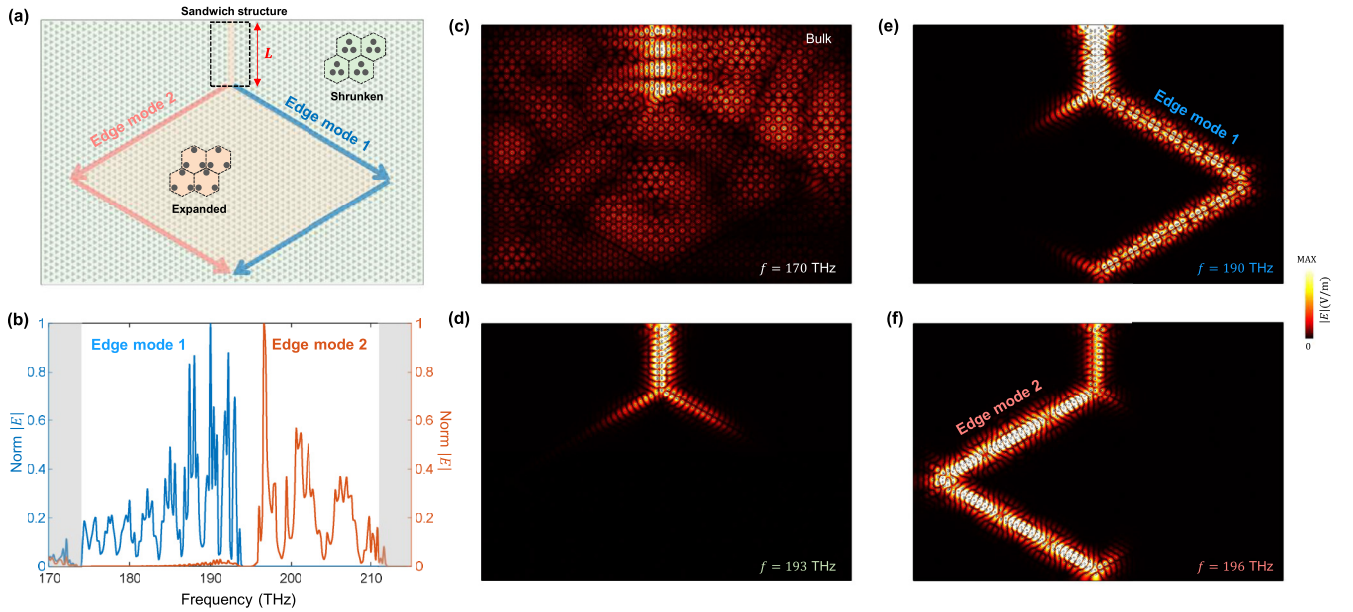


FIG. 2. (a) Scheme of a topological device composed of shrunken (green region) and expanded (orange region) kagome lattices, which contains two parts: a sandwich topological interface (marked by a black dashed box) and a diamondlike topological structure (the length of each side is $30a$). (b) Normalized electric field monitored by two probes placed at the output ports of the two branches in the diamondlike structure. (c)–(f) Field profiles for edge modes at different frequencies in our topological device.

case of trivial-nontrivial-trivial topology. Since the topological band inversion occurs only once at each inner boundary, each boundary supports a single edge mode. As a result, the bands of the two edge modes do not overlap, leading to the formation of a tiny band gap around 193 THz.

We also perform dispersion calculations for the topological interfaces 1 and 2, which contain inverted kagome lattices and exhibit a single boundary. As shown in Figs. 1(d) and 1(e), both of them exhibit two edge modes located within the topological band gap. However, the electric field of two edge modes in each topological interface is localized at the outer and inner boundaries, respectively. Note that the appearance of the outer edge mode is attributed to the application of periodic boundary conditions on the outer boundaries in the simulation model [28]. Correspondingly, the exchange of two kagome lattices leads to the reversion of the topological edge states due to the inversion of the nontrivial polarization difference [29]. The field distribution and dispersion relations indicate that the two distinct edge modes identified in the sandwich topological interface are related to the edge modes (localized at the inner boundary) of topological interfaces 1 and 2, respectively. The mode-matching behavior simplifies the process of coupling edge modes from the sandwich topological interface to other topological interfaces. Due to the distinct frequency ranges of the two edge modes, the coupling between different modes achieves a frequency-dependent filtering capability. In other words, the frequency division characteristic enables the realization of multifunctional on-chip topological photonic devices, which may find applications in areas such as optical transmission and light source generation.

Accordingly, we design a topological device composed of shrunken (green region) and expanded (orange region) kagome lattices, which contains two parts: a sandwich

topological interface (marked by a black dashed box) with a length of L and a diamondlike topological structure [Fig. 2(a)]. It is important to highlight that, in this design, the branches of the diamondlike structure exhibit distinct topological edge modes as a result of the mirror symmetry of the lattices. For the sandwich topological interface region, there are two allowed edge modes with different frequency ranges. However, for the diamondlike structure, the two branches correspond to topological interfaces 1 and 2, respectively. Therefore, the light can be efficiently transmitted to the left and right branches with the frequency range of $f > 193$ THz and $f < 193$ THz, respectively.

To get deeper insights into the characteristics of topological edge modes, we simulate the field profiles in this diamondlike structure at different frequencies. As shown in Figs. 2(c)–2(f), the energy couples to the opposite branch corresponding to different pump frequencies. We set two probes positioned at the output ports of two branches to monitor the field intensity. Figure 2(b) shows the simulated transmission spectra of the light, which clearly shows the frequency splitting functionality of our design. The presence of a frequency gap, characterized by the absence of power detected at either output port, results from the competition between the two edge modes. Accordingly, as shown in Fig. 2(d), the light does not engage with any branch at the specific frequency of around 193 THz. The result is consistent with the dispersion relation shown in Fig. 1(c). It is worth mentioning that this dichroic mirror behavior has the potential to facilitate a range of innovative topological functionalities.

B. Multiple OPPs in topological devices

Due to the fascinating functionalities of the diamondlike topological structure, we expect stable generation and

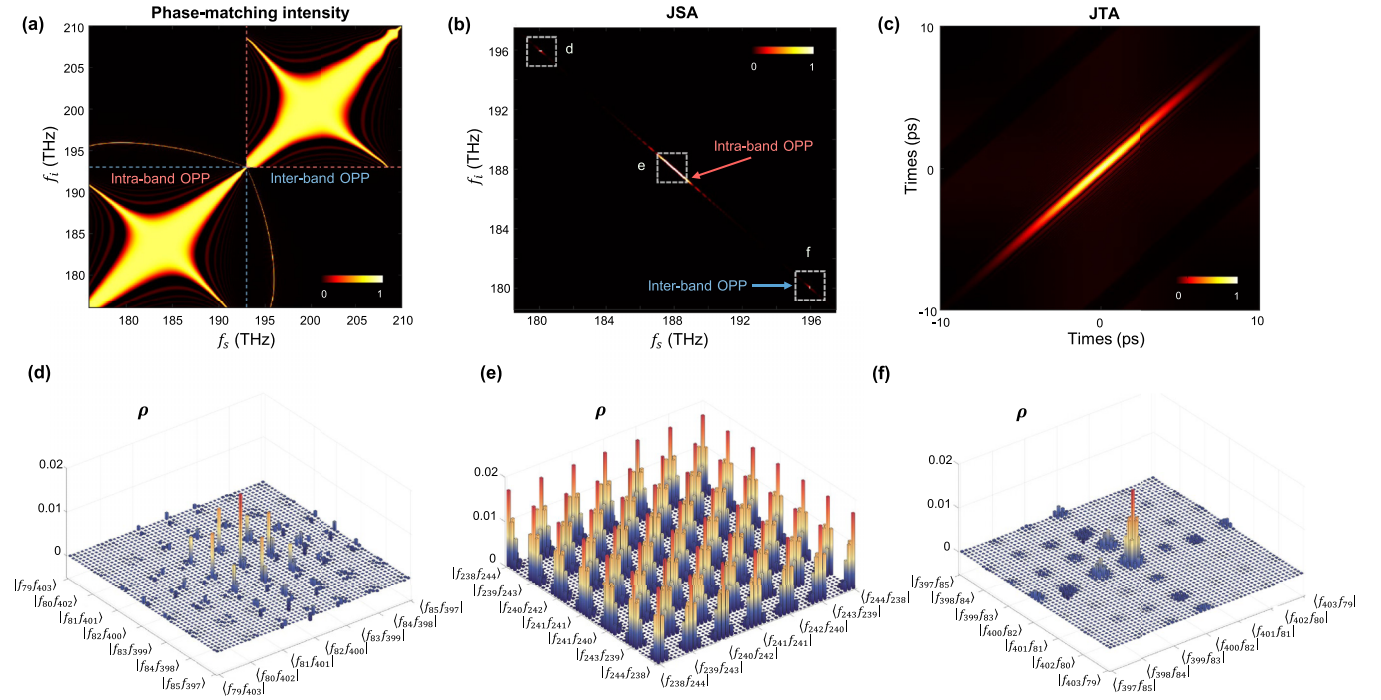


FIG. 3. (a) Phase-matching intensity distribution of FWM processes in the sandwich topological interface. (b) JSA distribution and (c) corresponding JTA distribution characterizing the biphoton state generated in the sandwich topological interface, where the color bar indicates the magnitude. (d)–(f) Three parts of the density matrix ρ of the quantum state corresponding to three regions (labeled by d, e, and f, respectively) in (b), where the coordinates in the horizontal plane denote different projection bases.

flexible manipulation of topological quantum states. Due to the absence of second-order nonlinearity of silicon, we only consider the FWM processes (third-order nonlinear effect). The nonlinear FWM processes generated in the sandwich topological interface can lead to the signal and idler photons. To ensure the topological transport of biphoton states, the frequencies of the pump, signal, and idler modes should be within the operation bandwidth of the topological edge modes. The energy and momentum conversion equations that govern the FWM processes are defined as $2\omega_p = \omega_s + \omega_i$ and $2k_p = k_s + k_i$, where $\omega_{p,s,i}$ and $k_{p,s,i}$ represent the frequencies and wave vectors of the pump, signal, and idler, respectively. In general, the Hamiltonian for the FWM process in the topological waveguide can be written as

$$\hat{H}_{\text{NL}} = \hat{H}_{\text{SPM}} + \hat{H}_{\text{XPM}} + \hat{H}_{\text{FWM}}, \quad (1)$$

where \hat{H}_{SPM} , \hat{H}_{XPM} , and \hat{H}_{FWM} denote the self-phase modulation (SPM), cross-phase modulation (XPM), and FWM processes, respectively. The SPM and XPM terms affect the oscillation process. Due to the frequency division of our diamondlike topological structure, the left and right branches correspond to the OPA process and entangled biphoton generation, respectively [30].

By matching the frequencies of FWM processes with the operating bandwidths of topological edge states, it becomes possible to implement topological protection of entangled biphoton states [16–18], and even quantum frequency combs [19,20]. The dispersion engineering of topological edge states offers a possible method for manipulating FWM processes within the topological band gap [16]. To satisfy the momentum conversion condition for FWM processes, the wave vector

mismatch $\Delta k = 2k_p - k_s - k_i$ must be taken into account. Note that the energy conversion of FWM processes is significantly improved when the wave vector mismatch satisfies $\Delta k = 0$. The phase-matching intensity of FWM processes is given by $\text{PM} = \text{sinc}(\frac{\Delta k L}{2})$, where L is the length of the topological interface [41].

The phase-matching intensity distribution of FWM processes in the sandwich topological interface is depicted in Fig. 3(a), demonstrating three cases of phase matching. The two main bright regions correspond to the intraband OPPs of the two edge modes themselves. However, besides the intraband OPP, an additional phase-matching case (bright curves) is also observed, corresponding to the interband OPP between two edge modes. The nonlinear interactions between two edge modes result in mode conversion, which can lead to significant correlations between different transverse modes.

By pumping the sandwich topological waveguide with the frequency of 188 THz, we can calculate the joint spectral amplitude (JSA) of the biphoton state generated from the FWM process. Such a biphoton state can be given by

$$|\Psi\rangle = \iint d\omega_s d\omega_i \mathcal{A}(\omega_s, \omega_i) \hat{a}_s^\dagger(\omega_s) \hat{a}_i^\dagger(\omega_i) |0\rangle, \quad (2)$$

where \hat{a}_s^\dagger and \hat{a}_i^\dagger are creation operators for photons and $\mathcal{A}(\omega_s, \omega_i)$ is the JSA. The JSA is governed by $\mathcal{A}(\omega_s, \omega_i) = \alpha(\frac{\omega_s + \omega_i}{2}) \text{sinc}(\frac{\Delta k L}{2})$, where the pump spectrum is $\alpha(\frac{\omega_s + \omega_i}{2})$ and joint phase-matching spectrum is $\text{sinc}(\frac{\Delta k L}{2})$. The pump is Gaussian with a frequency center of $f_p = 188$ THz and full width at half maximum of $\Delta f_p = 115$ GHz.

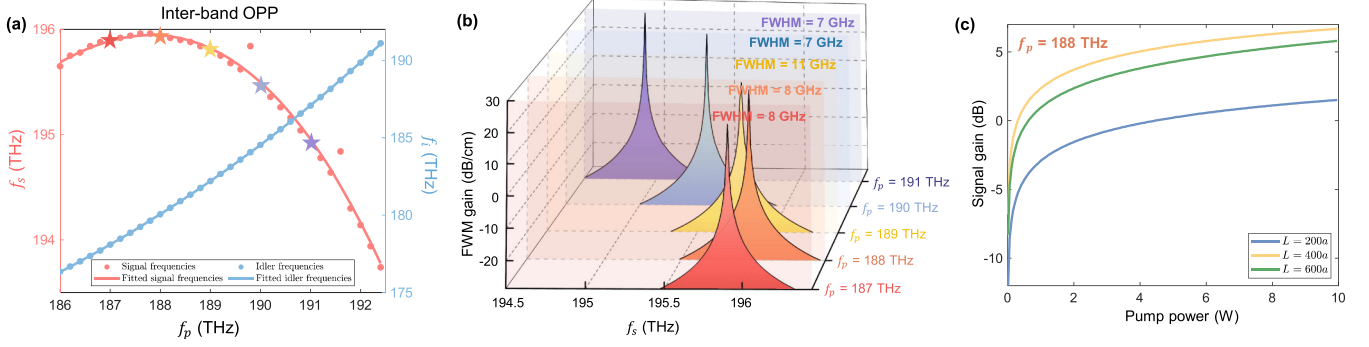


FIG. 4. (a) Frequencies of the signal and idler modes resulting from the interband OPP at different pump frequencies. (b) FWM gain coefficient corresponding to interband OPP at different pump frequencies for a $400a$ length topological waveguide (1 W pump power). (c) Signal gain as a function of pump power for the waveguide length with $L = 200a$, $400a$, and $600a$, respectively.

Consequently, the JSA characterizing the biphoton state generated in the sandwich topological interface is plotted in Fig. 3(b), where the main intensity region (corresponding to intraband OPP) along the diagonal axis denotes a strong signal-idler correlation in the frequency domain [16]. Notably, two additional bright spots are symmetrically located above and below the central line, indicating the presence of interband OPP. The spotlike phase-matching intensity distribution is also proven to be a perfect case for a heralded single photon generator [41] and, also, its purity can be improved by machine learning methods [42,43]. These points indicate the existence of frequency correlations resulting from the additional interband OPP interaction between edge mode 1 and edge mode 2. Note that the signal mode frequency is larger than 193 THz, so the generated signal can pass through the left branch while the generated idler passes through the right branch. The potential phase-matching conditions between two different topological edge states promise many effective solutions for manipulating photonic topological quantum states.

As a conjugate variable of the frequency, we can obtain the joint temporal amplitude (JTA) of the biphotons from the Fourier transform of the JSA by $\tilde{A}(t_s, t_i) = \mathcal{F}[A(\omega_i, \omega_s)]$ [43]. The peak intensity of the JTA is located at $\Delta\tau_y = \Delta\tau_z = 0$, indicating a relative phase value of $\phi = 0$ [Fig. 3(c)]. The biphoton state exhibits a signal-idler time correlation with a bandwidth of 10 ps.

Furthermore, we analyze the photonic topological quantum states by implementing quantum state tomography on a set of bases. We discretize the frequencies of the signal and idler modes in the JSA into 681 frequency modes, denoted as f_i , where $i = 1, 2, 3, \dots, 681$. Based on the JSA, we can calculate the density matrix of the quantum state by $\rho = |\Psi\rangle\langle\Psi|$, with projection bases of $|f_1 f_1\rangle, |f_1 f_2\rangle, |f_1 f_3\rangle, \dots, |f_{681} f_{681}\rangle$. Given its considerable size, we plot three parts of the density matrix (comprising 49 projection bases) in Figs. 3(d)–3(f) [corresponding to three dashed boxes in Fig. 3(b)]. The two density matrices [Figs. 3(d) and 3(f)] clearly demonstrate the emergence of the interband OPP.

C. Interband OPP: Tunable OPA

Our topological scheme supporting multiple OPPs provides a different approach to the manipulation of quantum functional devices. Here we implement an OPA by the FWM

with interband OPP, where the frequency division of the diamondlike structure leads to spatial separation of signal photons. This spatial separation behavior allows for the direct extraction of amplified optical signals since the generated signal could pass through the left branch of the diamondlike structure ($f_s > 193$ THz). We investigate the frequencies of the signal and idler modes resulting from the interband OPP with different pump frequencies. As shown in Fig. 4(a), the tunable range of the signal mode extends from 193.5 THz to 196 THz, achieving a tunable range of 2.5 THz.

Typically, signal and strong pump modes are coupled into the topological waveguide, where the signal power is amplified via degenerate FWM processes [44]. The FWM gain coefficient is given by $g = \sqrt{\gamma P_p \Delta k - (\Delta k/2)^2}$, where $\gamma = \omega_p n_2 / c A_{\text{eff}}$ is the effective nonlinearity of the topological waveguide, P_p is the pump power, n_2 is Kerr nonlinearity, A_{eff} is the nonlinear effective area, and c is the speed of light. The effective amplification in the waveguide requires strict adherence to a specific phase-matching condition due to the coherent nature of the parametric interaction. Figure 4(b) illustrates the FWM gain coefficient corresponding to interband OPP at different pump frequencies for a $400a$ length topological waveguide (1 W pump power). The interband OPP allows for a supernarrow bandwidth of high gain with a full width at half maximum (FWHM) of around 8 GHz. At the center frequency of the gain region, the FWM gain coefficient of up to 30 dB/cm can be achieved and the intensity of the FWM gain peak is constant during the tuning of the pump frequency. Such a narrow-bandwidth tunable OPA can be used to amplify signals from a single-photon source.

Consider a pump wave experiencing SPM, while cross-phase modulation XPM occurs in both signal and idler modes. Therefore, the nonlinear phase mismatch caused by SPM and XPM should be taken into account and the updated phase mismatch is given by $\Delta k_{\text{all}} = 2\gamma P_p - \Delta k$ [45]. Neglecting optical propagation loss, the observed signal gain generated via FWM for interband OPP can be written as [34]

$$G_s = \frac{P_s(L)}{P_s(0)} = 1 + \left(\frac{\gamma P_p}{g} \sinh(gL) \right)^2, \quad (3)$$

where $P_s(L)$ and $P_s(0)$ are the output and input signal powers, respectively. In Fig. 4(c), we plot the signal gain as a function of pump power for the waveguide length with

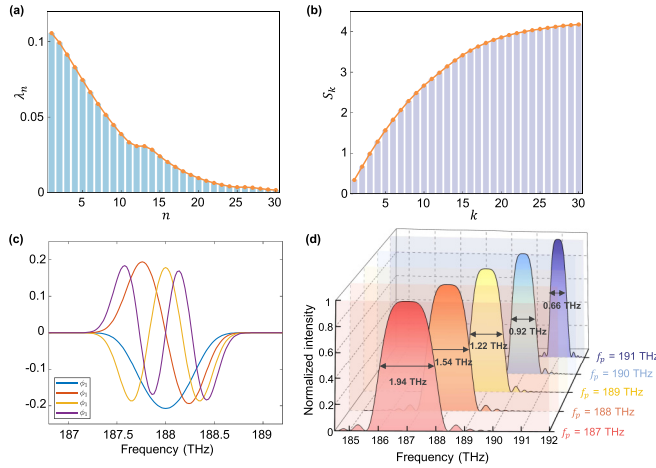


FIG. 5. Distribution of (a) normalized Schmidt coefficients λ_n and (b) entanglement entropy S_k for the biphoton state generated from intraband OPP. (c) Eigenfunctions ϕ_n ($n = 1, 2, 3, 4$) for the biphoton state. (d) Normalized two-photon spectral distribution with varying pump frequencies.

$L = 200a$, $400a$, and $600a$, respectively. For a topological waveguide with $L = 400a$, a peak signal gain of 5 dB can be achieved when the pump power exceeds 4 W. Note that when the gain of an OPA is large, the generated signal photons can be significantly amplified, reaching macroscopic levels through a phenomenon known as optical parametric generation. The expected number of photons at the output is given by $\langle n \rangle = \sinh^2(gL) \approx 0.25 \exp(2gL)$ [46]. The detailed quantum analysis of the OPA in our topological device is shown in Supplemental Sec. II [30]. Such a quantum OPA can be used in squeezing light detection [47] and optical homodyne measurement [48].

D. Intraband OPP: Entangled biphoton state generation

Furthermore, we can expect the generation and manipulation of a frequency entangled biphoton state derived from the intraband OPP. Note that all pump, signal, and idler modes can couple into the right branch of the diamondlike topological structure ($f_s, f_i < 193$ THz), which is convenient for extracting broadband entangled photon pairs directly at this branch. We use the Schmidt decomposition to evaluate the separability of the JSA without considering part of the phase information [37,49]. Figures 5(a) and 5(b) show the distributions of normalized Schmidt coefficients λ_n and entanglement entropy S_k , respectively. Note that the Schmidt coefficients λ_n indicate the probability of acquiring the n th quantum state. Nonzero coefficients (greater than 1) indicate the frequency entanglement [37,50]. Moreover, the entanglement entropy, denoted by $S_k = -\sum \lambda_n \log_2 \lambda_n$, and the Schmidt number, represented by $K = (\sum \lambda_n^2)^{-1}$, are reliable methods for measuring the degree of entanglement [49]. The entanglement of a topological quantum state can be verified by $S_k > 0$ or $K > 1$, where a higher value of S_k and K indicates a high-quality of frequency entanglement. For our topological quantum state, the calculated values for Schmidt number and entanglement entropy are $K = 16.24$ and $S_k = 4.42$, respectively, which

indicates the emergence of a high-quality frequency entangled biphoton state in the sandwich topological interface.

Due to the symmetry between the signal and idler photons, the eigenfunctions ϕ and ψ in the Schmidt decomposition have the same form. The initial four eigenfunctions ϕ_n ($n = 1, 2, 3, 4$) are shown in Fig. 5(c), which indicates the orthogonality of each basis function. Also, the number of photon pairs generated by the FWM process is given by

$$S(\omega) = \langle \Psi | a_s^\dagger a_i^\dagger a_i a_s | \Psi \rangle \\ = \frac{\eta^2}{c^2} \int d\omega_s \int d\omega_i |A(\omega_s, \omega_i)|^2, \quad (4)$$

where a_s and a_i are annihilation operators for photons and η is a constant term. Correspondingly, we calculate the normalized two-photon spectral distribution with pump at different frequencies. As shown in Fig. 5(d), the 3 dB bandwidths of the two-photon spectrum are 1.94, 1.54, 1.22, 0.92, and 0.66 THz, respectively, demonstrating the tunability of the spectral bandwidth. This high-dimensional topological quantum entangled state with tunable spectral bandwidth enables complex and large-scale quantum simulations and computations.

Alternatively, the single-photon purity associated with the factorization of biphoton states can be implemented by Schmidt decomposition. Purity plays a crucial role in achieving highly visible quantum interference between photons generated from the same source. In general, single-photon purity is expressed as $\text{Tr}(\hat{\rho}_s^2)$, where $\hat{\rho}_s = \text{Tr}_i(|\Psi\rangle\langle\Psi|)$ represents the density operator for the heralded single photon and Tr_i is the trace over the idler mode. The heralded single-photon purity, denoted as $\text{Tr}(\hat{\rho}_s^2)$, can be calculated by $\text{Tr}(\hat{\rho}_s^2) = K^{-1}$ [51]. Consequently, the single-photon purity for our topological quantum state is calculated to be 0.06, corresponding to a highly inseparable quantum state.

E. Robustness against disorders for FWM processes

To verify the topological protection of nonlinear FWM processes, we simulate the FWM process in the diamondlike topological structure with CW pump excitation [11,21] employing COMSOL MULTIPHYSICS software (see Methods). In our numerical model, we use a point source localized at the input port to excite topological edge modes. Notably, there is no input for the idler mode; the excitation of idler modes reveals the generation of stimulated FWM processes [11]. Here the frequencies of the pump, signal, and idler modes are chosen as $f_s = 196$ THz, $f_p = 188$ THz, and $f_i = 180$ THz, respectively. As depicted in Figs. 6(a)–6(c), the field profiles of topological edge modes at the idler frequency provide clear evidence of the simulated FWM process. Most importantly, due to their different frequencies, the pump and signal modes couple into the right branch of the diamondlike structure, while the generated idler mode couples into the left branch. As a result, the photon pairs are separated, with an idler photon being extracted during the FWM process.

In addition, we incorporate a diamondlike topological structure to extend the capacity of our system to a larger spatial domain, allowing for improved manipulation of the

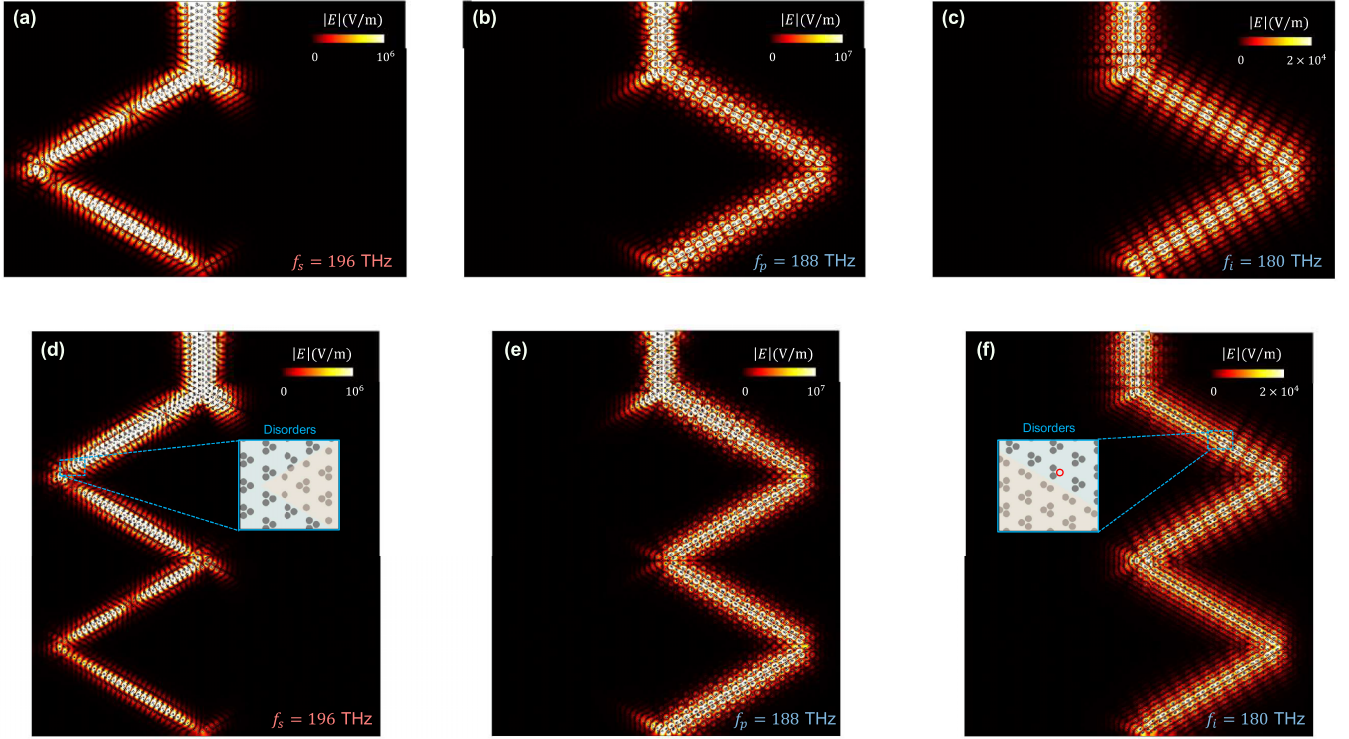


FIG. 6. Field profiles of the FWM process in the diamondlike topological structure at the frequencies of the (a) signal mode ($f_s = 196$ THz), (b) pump mode ($f_p = 188$ THz), and (c) idler mode ($f_i = 180$ THz), respectively. Field profiles of the stimulated FWM process in the expanded diamondlike topological structure at the frequencies of the (d) signal mode ($f_s = 196$ THz), (e) pump mode ($f_p = 188$ THz), and (f) idler mode ($f_i = 180$ THz), respectively. The red empty circle marked in (f) denotes the removed cylinder.

transmission routes of photonic topological quantum states. As shown in Figs. 6(d)–6(f), within the blue region, the position of a rod is randomly shifted by distances between $-0.1a$ and $0.2a$ (left branch) and a rod is randomly removed (right branch). The idler mode generated by FWM processes also shows strong localization along arbitrary topological boundaries. The results reveal that the topological nature of the QVH effect brings robustness to the FWM process against sharp bends and defects. These intriguing behaviors enable the manipulation of the two-photon state's path and the flexible extraction of individual photons.

III. CONCLUSION

In this work, we demonstrate on-chip topological quantum optical devices capable of performing multiple functions including OPA and entangled biphoton generation. We show that there exist two distinct edge modes corresponding to different frequency ranges in the sandwich topological interface. By employing a diamond structure, we can couple these two edge modes into separate branches to achieve the separation of spatial modes. Due to the coexistence of two edge modes, the FWM process enables two types of OPPs, corresponding to interband and intraband cases, respectively. More importantly, thanks to distinct transmission paths of the edge modes, these two OPPs can individually facilitate quantum OPA and the generation of continuous frequency-entangled photon pairs along separate branches. In addition, these quantum processes

exhibit topological protection properties, showing robustness to defects and sharp bends. Our proposal offers enhanced possibilities for on-chip robust, multifunctional topological quantum devices.

IV. METHODS

A. Numerical simulation

We use the finite-element method solver COMSOL MULTIPHYSICS to perform numerical simulations. The band diagrams [Fig. 1(b)] and dispersion curves [Figs. 1(c)–1(e)] of topological photonic crystals are calculated by solving the eigenfrequencies with periodic boundary conditions. Here we consider the field profiles of transverse magnetic (TM) polarization modes. In the simulation of the electric field profile [Figs. 2(c)–2(f)], we construct the diamondlike topological structure in the frequency domain solver and then use a point source to excite the edge states. The simulated nonlinear FWM processes (Fig. 6) are performed by using the third-order nonlinearity of silicon $\chi^{(3)} = 5 \times 10^{-18} \text{ m}^2/\text{V}^2$. The FWM process in the sandwich topological interface can be described by

$$\begin{aligned}
 \mathbf{P}_p(\omega_s + \omega_i - \omega_p) &= 6\epsilon_0\chi^{(3)}E_sE_iE_p^*, \\
 \mathbf{P}_s(\omega_p + \omega_p - \omega_i) &= 3\epsilon_0\chi^{(3)}E_pE_pE_i^*, \\
 \mathbf{P}_i(\omega_p + \omega_p - \omega_s) &= 3\epsilon_0\chi^{(3)}E_pE_pE_s^*,
 \end{aligned} \tag{5}$$

where ε_0 is the vacuum permittivity and $\mathbf{P}_{p,s,i}$ and $E_{p,s,i}$ are the polarization and electric field of the pump, signal, and idler, respectively. The frequencies of the pump, signal, and idler modes are chosen as $f_s = 196$ THz, $f_p = 188$ THz, and $f_i = 180$ THz, respectively. A point source localized at the input port is used to excite the pump and signal modes, while there is no input for the idler mode. Due to the coupling of three electromagnetic modes at the pump and signal frequencies, the excitation of idler modes reveals the generation of stimulated FWM processes [11,21].

B. Theoretical analysis of interband OPP

In our diamondlike topological device, the interband OPP in the sandwich topological interface leads to an OPA process. Note that only the signal mode can be coupled into the left branch, which is more beneficial for the extraction of the amplified signal. From the nonlinear Hamiltonian [Eq. (2)], we can derive the Heisenberg equations for the pump, signal, and idler modes [11]. By substituting the operators in the Heisenberg equations with classical light fields, the coupled equations for these three modes can be given by

$$\begin{aligned}\frac{dA_p}{dx} &= i\gamma\{[|A_p|^2 + 2(|A_s|^2 + |A_i|^2)]A_p \\ &\quad + 2A_s A_i A_p^* \exp(i\Delta kx)\}, \\ \frac{dA_s}{dx} &= i\gamma\{[|A_s|^2 + 2(|A_i|^2 + |A_p|^2)]A_s \\ &\quad + A_i^* A_p^2 \exp(-i\Delta kx)\},\end{aligned}$$

$$\begin{aligned}\frac{dA_i}{dx} &= i\gamma\{[|A_i|^2 + 2(|A_s|^2 + |A_p|^2)]A_i \\ &\quad + A_s^* A_p^2 \exp(-i\Delta kx)\},\end{aligned}\quad (6)$$

where $A_j(x)$, $j \in \{p, s, i\}$ is the amplitude of the light field. Solving the coupled equations enables the amplification of a weak signal as it propagates along the topological waveguide; we can get an analytical solution

$$P_s(L) = P_s(0) \left(1 + \left[\frac{\gamma P_p}{g} \sinh(gL) \right]^2 \right). \quad (7)$$

With this equation, we can calculate the power of the signal light after it has propagated a distance L through the topological waveguide. Therefore, the signal gain can be given by [34]

$$G_s = \frac{P_s(L)}{P_s(0)} = 1 + \left(\frac{\gamma P_p}{g} \sinh(gL) \right)^2. \quad (8)$$

ACKNOWLEDGMENTS

This work is supported by the National Key Research and Development Program of China (2021YFB2800401), Key-Area Research and Development Program of Guangdong Province (Grant No. 2018B030325002), the National Natural Science Foundation of China (Grant No. 62075129), the SJTU Pinghu Institute of Intelligent Optoelectronics (Grant No. 2022SPIOE204), and the Sichuan Provincial Key Laboratory of Microwave Photonics (2023-04).

The authors declare no competing interests.

-
- [1] G. Moody, L. Chang, T. J. Steiner, and J. E. Bowers, Chip-scale nonlinear photonics for quantum light generation, *AVS Quantum Sci.* **2**, 041702 (2020).
- [2] J. L. O'Brien, Optical quantum computing, *Science* **318**, 1567 (2007).
- [3] L. Caspani, C. Xiong, B. J. Eggleton, D. Bajoni, M. Liscidini, M. Galli, R. Morandotti, and D. J. Moss, Integrated sources of photon quantum states based on nonlinear optics, *Light Sci. Appl.* **6**, e17100 (2017).
- [4] P. Sibson, C. Erven, M. Godfrey, S. Miki, T. Yamashita, M. Fujiwara, M. Sasaki, H. Terai, M. G. Tanner, C. M. Natarajan *et al.*, Chip-based quantum key distribution, *Nat. Commun.* **8**, 13984 (2017).
- [5] X. Lu, Q. Li, D. A. Westly, G. Moille, A. Singh, V. Anant, and K. Srinivasan, Chip-integrated visible-telecom entangled photon pair source for quantum communication, *Nat. Phys.* **15**, 373 (2019).
- [6] A. Orioux and E. Diamanti, Recent advances on integrated quantum communications, *J. Opt.* **18**, 083002 (2016).
- [7] S. Pirandola, B. R. Bardhan, T. Gehring, C. Weedbrook, and S. Lloyd, Advances in photonic quantum sensing, *Nat. Photon.* **12**, 724 (2018).
- [8] C. L. Degen, F. Reinhard, and P. Cappellaro, Quantum sensing, *Rev. Mod. Phys.* **89**, 035002 (2017).
- [9] Y. Wang, K. D. Jöns, and Z. Sun, Integrated photon-pair sources with nonlinear optics, *Appl. Phys. Rev.* **8**, 011314 (2021).
- [10] Q. Yan, X. Hu, Y. Fu, C. Lu, C. Fan, Q. Liu, X. Feng, Q. Sun, and Q. Gong, Quantum topological photonics, *Adv. Opt. Mater.* **9**, 2001739 (2021).
- [11] J. W. You, Z. Lan, Q. Ma, Z. Gao, Y. Yang, F. Gao, M. Xiao, and T. J. Cui, Topological metasurface: From passive toward active and beyond, *Photon. Res.* **11**, B65 (2023).
- [12] S. Barik, A. Karasahin, C. Flower, T. Cai, H. Miyake, W. DeGottardi, M. Hafezi, and E. Waks, A topological quantum optics interface, *Science* **359**, 666 (2018).
- [13] S. Mittal, E. A. Goldschmidt, and M. Hafezi, A topological source of quantum light, *Nature (London)* **561**, 502 (2018).
- [14] S. Mittal, V. V. Orre, E. A. Goldschmidt, and M. Hafezi, Tunable quantum interference using a topological source of indistinguishable photon pairs, *Nat. Photon.* **15**, 542 (2021).
- [15] Y. Chen, X.-T. He, Y.-J. Cheng, H.-Y. Qiu, L.-T. Feng, M. Zhang, D.-X. Dai, G.-C. Guo, J.-W. Dong, and X.-F. Ren, Topologically protected valley-dependent quantum photonic circuits, *Phys. Rev. Lett.* **126**, 230503 (2021).
- [16] Z. Jiang, Y. Ding, C. Xi, G. He, and C. Jiang, Topological protection of continuous frequency entangled biphoton states, *Nanophotonics* **10**, 4019 (2021).
- [17] T. Dai, Y. Ao, J. Bao, J. Mao, Y. Chi, Z. Fu, Y. You, X. Chen, C. Zhai, B. Tang *et al.*, Topologically protected quantum entanglement emitters, *Nat. Photon.* **16**, 248 (2022).
- [18] S. Afzal, T. J. Zimmerling, M. Rizvandi, M. Taghavi, T. Hrushevskiy, M. Kaur, V. Van, and S. Barzanjeh, Bright

- quantum photon sources from a topological floquet resonance, [arXiv:2308.11451](https://arxiv.org/abs/2308.11451).
- [19] Z. Jiang, Y. Chen, C. Jiang, and G. He, Generation of quantum optical frequency combs in topological resonators, *Adv. Quantum Technol.* **7**, 2300354 (2024).
- [20] Z. Jiang, H. Wang, Y. Yang, Y. Shen, B. Ji, Y. Chen, Y. Zhang, L. Sun, Z. Wang, C. Jiang *et al.*, On-chip topological transport of optical frequency combs in silicon-based valley photonic crystals, [arXiv:2310.15629](https://arxiv.org/abs/2310.15629).
- [21] J. W. You, Z. Lan, and N. C. Panoiu, Four-wave mixing of topological edge plasmons in graphene metasurfaces, *Sci. Adv.* **6**, eaaz3910 (2020).
- [22] D. Smirnova, S. Kruk, D. Leykam, E. Melik-Gaykazyan, D.-Y. Choi, and Y. Kivshar, Third-harmonic generation in photonic topological metasurfaces, *Phys. Rev. Lett.* **123**, 103901 (2019).
- [23] T. Dai, Y. Ao, J. Mao, Y. Yang, Y. Zheng, C. Zhai, Y. Li, J. Yuan, B. Tang, Z. Li *et al.*, Non-hermitian topological phase transitions controlled by nonlinearity, *Nat. Phys.* **20**, 101 (2023).
- [24] D. Smirnova, D. Leykam, Y. Chong, and Y. Kivshar, Nonlinear topological photonics, *Appl. Phys. Rev.* **7**, 021306 (2020).
- [25] Z. Jiang, L. Zhou, W. Li, Y. Li, L. Feng, T. Wu, C. Jiang, and G. He, Topological dissipative Kerr soliton combs in a valley photonic crystal resonator, *Phys. Rev. B* **108**, 205421 (2023).
- [26] S. Mittal, G. Moille, K. Srinivasan, Y. K. Chembo, and M. Hafezi, Topological frequency combs and nested temporal solitons, *Nat. Phys.* **17**, 1169 (2021).
- [27] A. Vakulenko, S. Kiriushchikina, M. Wang, M. Li, D. Zhirihin, X. Ni, S. Guddala, D. Korobkin, A. Alù, and A. B. Khanikaev, Near-field characterization of higher-order topological photonic states at optical frequencies, *Adv. Mater.* **33**, 2004376 (2021).
- [28] M. Li, D. Zhirihin, M. Gorchach, X. Ni, D. Filonov, A. Slobozhanyuk, A. Alù, and A. B. Khanikaev, Higher-order topological states in photonic kagome crystals with long-range interactions, *Nat. Photon.* **14**, 89 (2020).
- [29] M. Ezawa, Higher-order topological insulators and semimetals on the breathing kagome and pyrochlore lattices, *Phys. Rev. Lett.* **120**, 026801 (2018).
- [30] See Supplemental Material at <http://link.aps.org/supplemental/10.1103/PhysRevB.109.174110> for (i) topological kagome lattice, (ii) theoretical analysis of two opps in topological devices, and (iii) implementing multiple opps in honeycomb lattices, which includes Refs. [31–40].
- [31] X. Ni, M. Weiner, A. Alu, and A. B. Khanikaev, Observation of higher-order topological acoustic states protected by generalized chiral symmetry, *Nat. Mater.* **18**, 113 (2019).
- [32] R. D. King-Smith and D. Vanderbilt, Theory of polarization of crystalline solids, *Phys. Rev. B* **47**, 1651 (1993).
- [33] A. L. Gaeta, M. Lipson, and T. J. Kippenberg, Photonic-chip-based frequency combs, *Nat. Photon.* **13**, 158 (2019).
- [34] J. Hansryd, P. A. Andrekson, M. Westlund, J. Li, and P.-O. Hedekvist, Fiber-based optical parametric amplifiers and their applications, *IEEE J. Sel. Top. Quantum Electron.* **8**, 506 (2002).
- [35] G. Cappellini and S. Trillo, Third-order three-wave mixing in single-mode fibers: exact solutions and spatial instability effects, *J. Opt. Soc. Am. B* **8**, 824 (1991).
- [36] R. Stolen and J. Bjorkholm, Parametric amplification and frequency conversion in optical fibers, *IEEE J. Quantum Electron.* **18**, 1062 (1982).
- [37] C. K. Law, I. A. Walmsley, and J. H. Eberly, Continuous frequency entanglement: effective finite hilbert space and entropy control, *Phys. Rev. Lett.* **84**, 5304 (2000).
- [38] Y. Yang, Y. Yamagami, X. Yu, P. Pitchappa, J. Webber, B. Zhang, M. Fujita, T. Nagatsuma, and R. Singh, Terahertz topological photonics for on-chip communication, *Nat. Photon.* **14**, 446 (2020).
- [39] J. Lu, C. Qiu, L. Ye, X. Fan, M. Ke, F. Zhang, and Z. Liu, Observation of topological valley transport of sound in sonic crystals, *Nat. Phys.* **13**, 369 (2017).
- [40] J. Noh, S. Huang, K. P. Chen, and M. C. Rechtsman, Observation of photonic topological valley Hall edge states, *Phys. Rev. Lett.* **120**, 063902 (2018).
- [41] P. J. Mosley, J. S. Lundeen, B. J. Smith, P. Wasylczyk, A. B. U'Ren, C. Silberhorn, and I. A. Walmsley, Heralded generation of ultrafast single photons in pure quantum states, *Phys. Rev. Lett.* **100**, 133601 (2008).
- [42] C. Cui, R. Arian, S. Guha, N. Peyghambarian, Q. Zhuang, and Z. Zhang, Wave-function engineering for spectrally uncorrelated biphotons in the telecommunication band based on a machine-learning framework, *Phys. Rev. Appl.* **12**, 034059 (2019).
- [43] W.-H. Cai, Y. Tian, S. Wang, C. You, Q. Zhou, and R.-B. Jin, Optimized design of the lithium niobate for spectrally-pure-state generation at mir wavelengths using metaheuristic algorithm, *Adv. Quantum Technol.* **5**, 2200028 (2022).
- [44] J. Riemensberger, N. Kuznetsov, J. Liu, J. He, R. N. Wang, and T. J. Kippenberg, A photonic integrated continuous-travelling-wave parametric amplifier, *Nature (London)* **612**, 56 (2022).
- [45] M. A. Foster, A. C. Turner, J. E. Sharping, B. S. Schmidt, M. Lipson, and A. L. Gaeta, Broad-band optical parametric gain on a silicon photonic chip, *Nature (London)* **441**, 960 (2006).
- [46] L. Ledezma, R. Sekine, Q. Guo, R. Nehra, S. Jahani, and A. Marandi, Intense optical parametric amplification in dispersion-engineered nanophotonic lithium niobate waveguides, *Optica* **9**, 303 (2022).
- [47] R. Nehra, R. Sekine, L. Ledezma, Q. Guo, R. M. Gray, A. Roy, and A. Marandi, Few-cycle vacuum squeezing in nanophotonics, *Science* **377**, 1333 (2022).
- [48] Y. Shaked, Y. Michael, R. Z. Vered, L. Bello, M. Rosenbluh, and A. Pe'er, Lifting the bandwidth limit of optical homodyne measurement with broadband parametric amplification, *Nat. Commun.* **9**, 609 (2018).
- [49] M. Kues, C. Reimer, P. Roztocky, L. R. Cortés, S. Sciara, B. Wetzels, Y. Zhang, A. Cino, S. T. Chu, B. E. Little *et al.*, On-chip generation of high-dimensional entangled quantum states and their coherent control, *Nature (London)* **546**, 622 (2017).
- [50] M. Erhard, M. Krenn, and A. Zeilinger, Advances in high-dimensional quantum entanglement, *Nat. Rev. Phys.* **2**, 365 (2020).
- [51] L. E. Vicent, A. B. U'Ren, R. Rangarajan, C. I. Osorio, J. P. Torres, L. Zhang, and I. A. Walmsley, Design of bright, fiber-coupled and fully factorable photon pair sources, *New J. Phys.* **12**, 093027 (2010).